Published in final edited form as:

Mol Pharm. 2019 May 06; 16(5): 2028–2036. doi:10.1021/acs.molpharmaceut.9b00010.

Site-Specific Immuno-PET Tracer to Image PD-L1

Haley L. Wissler[†,§], **Emily B. Ehlerding**[‡,§], **Zhigang Lyu**[†], **Yue Zhao**[†], **Si Zhang**[†], **Anisa Eshraghi**[†], **Zakey Yusuf Buuh**[†], **Jeffrey C. McGuth**[†], **Yifu Guan**[†], **Jonathan W. Engle**[‡], **Sarah J. Bartlett**[†], **Vincent A. Voelz**[†], **Weibo Cai**[‡,*], and **Rongsheng E. Wang**[†,*]

[†]Department of Chemistry, Temple University, 1901 N. 13th Street, Philadelphia, Pennsylvania 19122, United States

[‡]Departments of Radiology and Medical Physics, University of Wisconsin-Madison, Madison, Wisconsin 53705, United States

Abstract

The rapid ascension of immune checkpoint blockade treatments has placed an emphasis on the need for viable, robust, and noninvasive imaging methods for immune checkpoint proteins, which could be of diagnostic value. Immunoconjugate-based positron emission tomography (immuno-PET) allows for sensitive and quantitative imaging of target levels and has promising potential for the noninvasive evaluation of immune checkpoint proteins. However, the advancement of immuno-PET is currently limited by available imaging tools, which heavily rely on full-length IgGs with Fc-mediated effects and are heterogeneous mixtures upon random conjugation with chelators for imaging. Herein, we have developed a site-specific αPD-L1 Fab conjugate with the chelator 1,4,7-triazacyclononane-N,N',N''-triacetic acid (NOTA), enabling radiolabeling for PET imaging, using the amber suppression-mediated genetic incorporation of unnatural amino acid (UAA), *p*-azidophenylalanine. This Fab conjugate is homogeneous and demonstrated tight binding toward the PD-L1 antigen in vitro. The radiolabeled version, ^{64}Cu-NOTA-αPD-L1, has been employed in PET imaging to allow for effective visualization and mapping of the biodistribution of PD-L1 in two normal mouse models, including the capturing of different PD-L1 expression levels in the spleens of the different mouse types. Follow-up in vivo blocking studies and ex vivo fluorescent staining further validated specific tissue uptakes of the imaging agent. This approach illustrates the utility of UAA-based site-specific Fab conjugation as a general strategy for making sensitive PET imaging probes, which could facilitate the elucidation of the roles of a wide variety of immune checkpoint proteins in immunotherapy.

Graphical Abstract

[*]**Corresponding Authors** wcai@uwhealth.org. Phone: 608-262-1749 (W.C.); rosswang@temple.edu. Phone: 215-204-1855 (R.E.W.).
[§]H.L.W. and E.B.E. contributed equally.

Supporting Information

The Supporting Information is available free of charge on the ACS Publications website at DOI:10.1021/acs.molpharmaceut.9b00010. Chemical synthesis, cloning of antibody expression vectors, antibody sequences, expression and purification of antibody Fab fragments, in silico screening of mutation sites on αPD-L1 Fab, site-specific conjugation and purification of Fab–NOTA conjugates, ELISA assay, radiolabeling, in vivo PET imaging, LC–MS and NMR analysis of compound **4** (Figure S1), SDS-PAGE analysis of antibody Fab fragments (Figure S2), ESI-MS characterization of antibody conjugate (Figure S3), in vivo PET imaging studies (Figure S4), ex vivo biodistribution (Figure S5) (PDF)

The authors declare no competing financial interest.

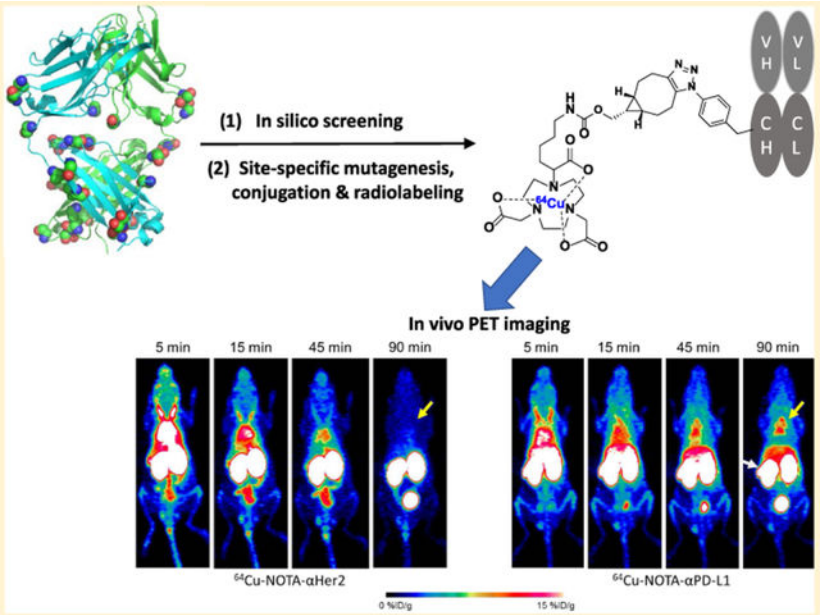

Keywords

antibody; immune checkpoint; immunotherapy; PD-L1; site-specific; positron emission tomography; unnatural amino acid

INTRODUCTION

Checkpoint inhibitor-based cancer immunotherapy has recently emerged as a pillar of effective treatment to control tumor growth and dissemination.[1,2] The discovery of multiple immune checkpoint mechanisms such as program death-ligand 1 (PD-L1), programmed cell death protein 1 (PD-1), and cytotoxic T-lymphocyte-associated protein 4 (CTLA-4) has facilitated the understanding of how tumor cells bypass the attack of immune systems.[3] Therapeutic treatments utilizing immune checkpoint inhibitors would “wake up” the previously suppressed immune cells and activate them to attack tumor cells.[3] Thus, these inhibitors, such as antibodies, have become first-line therapies for different tumor types.[1,3] Yet, heterogeneous outcomes in clinical responses, frequent toxicity, and adverse effects necessitate the development of new methods for the prognosis and monitoring of patient responses.[1,2,4–8] A noninvasive strategy to comprehensively monitor the expression of immune checkpoint proteins may help elucidate their roles in immunotherapeutic responses and potentially be useful in patient selection and treatment monitoring.[4,9–13] Molecular imaging, especially positron emission tomography using antibodies conjugated with radionuclides (immuno- PET), allows for accurate and noninvasive evaluation of target levels.[14–16] Due to the high sensitivity and resolution, immuno-PET has been successfully applied to interrogate the relationship between tissue uptake and clinical responses toward antibody treatment.[17–19] Thus, immuno-PET could be a crucial tool to test the biomarker hypothesis of immune checkpoint proteins for immunotherapy.[15,16,20]

Despite previous PET imaging efforts for immune checkpoint proteins,[9–11,20–26] most immune checkpoint-based PET probes rely on full-length IgG antibodies,[10,21,23,24] which have limited tissue/tumor penetrance. Fab fragments, on the other hand, retain the binding of the antibody but are devoid of the Fc effector domain. The resulting shorter circulation half-lives and less off-target-related background signals make them ideal probe candidates.[27,28] Yet, few Fab-based PET probes have been developed so far.[27,28] More importantly, common antibody probes have been synthesized via random coupling of natural amino acids with chelators, resulting in heterogeneous constructs with suboptimal stabilities, efficacies, and pharmacological properties.[29,30] Early studies with cysteine-based site-specific immunoconjugates revealed higher target-to-background imaging intensity ratios than random conjugates,[30] demonstrating the positive effects on in vivo performance of precise control of conjugation sites and stoichiometry. Yet, the suboptimal biological stability of the resulting maleimdyl thioether bonds largely limited its broad applications.[30] Another cysteine-based approach, expressed protein ligation (EPL), could result in relatively stable coupling, but the feasible site is mainly limited to C-terminals which may not render the most stable conjugates.[31] On the other hand, application of EPL to multiple modifications within the protein sequence would be technically demanding.[32,33] Recently, another site-specific conjugation strategy emerged, with the amber suppression-mediated genetic incorporation of unnatural amino acids (UAAs) during the translation of recombinant proteins.[33,34] In this approach, the amber stop codon employs paired orthogonal amino-acyl transferase and iso-tRNA to incorporate the desired UAA site specifically into proteins including the recombinant anti-body.[33,34] Antibodies incorporating UAAs, such as *p*-acetylphenylalanine (pAcF), can be coupled to small molecules of interest via a stable linkage,[29,35,36] generating site-specific therapeutics in high yields. The UAA conjugates as therapeutic candidates have demonstrated superior in vivo efficacy, stability, and toxicology profiles to the cysteine conjugates.[34,37,38] Nevertheless, UAA-incorporated immunoconjugates have rarely been applied to PET imaging.[29,39]

To this end, we have developed a site-specific immuno-PET probe by incorporating one UAA, *p*-azidophenylalanine (pAzF), into antibody Fab fragments. Using the antibody against the popularly studied immune checkpoint protein PD-L1, as an example, we demonstrated for the first time the generation, optimization, and in vivo PET imaging of a UAA-based site-specific Fab conjugate with 1,4,7-triazacyclononane-*N*,*N*′,*N*″-triacetic acid (NOTA).

EXPERIMENTAL SECTION

Materials.

Reagents and solvents were obtained directly from commercial resources such as Thermo Fisher, VWR, and Sigma-Aldrich and were used without further purification. Analytical thin-layer chromatography was performed with EMD Chemicals Silica gel 60 F_{254} plates, the chemicals which were visualized by UV lamp (Chemglass Life Sciences) at 254/365 nm, $KMnO_4$ staining, or phosphomolybdic acid staining. For purification, flash column chromatography was performed with silica gel grade 60 (230–400 mesh, Fisher Scientific). Preparative high-performance liquid chromatography (HPLC) was carried out on Waters

1525 series equipped with a 2489 UV/vis detector, 1525 binary pump, and a XBridge Prep C18 column (5 μm, 19 × 250 mm^2). Solvent A was water/0.5% trifluoroacetic acid, and solvent B was acetonitrile. For mass spectrometry (MS) analysis, regular liquid chromatography-mass spectrometry (LC-MS) was performed on Agilent 1100 series. High-resolution LC–MS analysis was done on an Agilent 6520 Accurate-Mass Quadrupole-Time-of-Flight (Q-TOF) coupled with an electrospray ionization (ESI) source. A zorbax 300SB-C8 column (5 μm, 4.6 × 50 mm^2) was used. For acquisition of NMR spectroscopy, ^{1}H NMR and ^{13}C NMR were recorded on 400 or 500 MHz Bruker Advance. The data were processed with the MestReNova Software, measuring signal shifts in parts per million (ppm) downfield from the internal standard tetramethylsilane.

Methods.

Please see the Supporting Information for experimental details.

RESULTS AND DISCUSSION

Synthesis of the NOTA–BCN Linker.

We began by designing and synthesizing the PET chelator. Copper-64 as a metallic radionuclide garners interest due to its favorable physical properties, appropriate half-life, and ease of production.[40–43] Among the available macrocyclic chelates, the NOTA series have been reported to possess superior chelation ability.[40] Notably, the hexadentate NOTA derivative with 1-branched substitution (3p-C-NOTA) had higher radiolabeling efficiency and stability than the other NOTA derivatives[40] but has yet to be utilized for immuno-PET.[44–46] Thus, we set out to synthesize a similar NOTA derivative with the termini modified with bicyclo[6.1.0]non-4-yne (BCN) for strain-promoted azide–alkyne cycloaddition (SPAAC) conjugation.[47] 6-Benzamidohexanoic acid was first reacted with benzoyl chloride to afford protected linker compound **1** (Scheme 1).[48] Bromination followed by methylation resulted in methyl 6-benzamido-2-bromohexanoate (compound **2**). The 1,4,7-triazacyclononane (TACN) moiety was introduced by reacting the linker compound **2** with TACN-1,7-bis(*t*-butyl acetate) in the presence of potassium carbonate.[45,48] The resulting intermediate was hydrolyzed under strong acid conditions to generate the amine-derivatized NOTA compound **3**. A final coupling of **3** with the BCN-succinimidyl ester, followed by HPLC purification, afforded the NOTA–BCN linker (compound **4**) with >95% purity, as shown by LC–MS analysis (Supporting Information Figure S1).

Design and Synthesis of Anti-PD-L1 Fab Mutant.

Compared to IgGs, antibody Fab fragments possess a small protein size, thereby improving tissue penetrance, and the removal of the Fc portion avoids unwanted effector effects.[27,28] Its shorter biological half-life enables labeling with shorter-lived radionuclides such as copper-64, which taken together should lead to improved signal-to-background ratios at earlier time points.[27] These unique characteristics make them not only suitable for therapeutic development[49,50] but also as ideal imaging agents,[27] warranting a detailed test of the site-specific incorporation of UAA. Among all of the available immune checkpoint proteins, PD-L1 appears to be the most studied due to its broad and dynamic expression profile and its potential correlation with prognosis and therapy responsiveness.

[10,20,21,23,24,26] Hence, we picked the sequences coding for the variable regions of the αPD-L1 antibody avelumab, which has been clinically approved for treating gastric cancer and Merkel-cell carcinoma and is also human–mouse crossreactive.[51] The plasmid (pBAD_αPD-L1) was constructed to harbor the heavy- and lambda light chain genes of the Fab fragment following a stll signal peptide.[36,52] The wild type αPD-L1 Fab was expressed in *Escherichia coli*, with a yield of 4.2 mg/L in shake flask cultures. Sodium dodecyl sulfate/polyacrylamide gel electrophoresis (SDS/PAGE) analysis showed that the Fab fragment migrated as a single band, with >95% purity and a molecular mass of ~45 kDa (Figure S2).

The site-specific labeling strategy based on the genetic incorporation of UAA allows one to explore various conjugates with different geometries and stabilities.[36,52] Previous studies on a couple of mutation sites have resulted in Fab fragments of significantly different yields.[36] Nevertheless, there has been no systematic study done to determine the optimal conjugation site. To this end, we selected 23 possible sites on αPD-L1 Fab, which are surface-exposed, distal to binding sites, and are in flexible loops (Figure 1A). In silico screening was performed using the RosettaBackrub algorithm to predict the viability of single point mutations at the selected sites (Figure 2). The results suggested that mutations at HC-K129 would be most favorably tolerated (Figure 2). Notably, the site HC-K129 has been experimentally explored before to be an ideal conjugation site for pAcF with high expression yield and little interference with antigen binding.[36,52,53] As a negative control in our experimental validation of the screening results, LC-V202 was picked for amber suppression as well. Despite the previous site-specific incorporation of pAcF for oxime coupling,[36] we decided to employ the incorporation of pAzF for strain-promoted SPAAC in this study. Compared to oxime coupling, the strain-promoted SPAAC conjugation is more bioorthogonal and can proceed efficiently at neutral pH.[39,54,55] Although there are few reports in regards to its incorporation onto antibodies,[54] electron-deficient aryl azides, such as pAzF, have been shown to greatly accelerate the SPAAC reaction.[47]

Therefore, we performed site-directed mutation of HC-K129 or LC-V202 to the TAG codon and co-transformed each pBAD plasmid into the DH10B strain along with a plasmid (pULTRA_pCNF)[56] that encodes the polyspecific Mj-tRNA/tyrosyl-tRNA synthetase pair evolved to incorporate the pAzF UAA. The expression yield for αPD-L1 Fab mutant (HC K129X, X = pAzF) was 2.5 mg/L, whereas the yield for αPD-L1 Fab (LC V202X, X = pAzF) was only 0.04 mg/L. This significant difference is consistent with the in silico screening results and emphasizes the importance of optimizing the labeling site. In parallel, we also cloned and expressed αHER2 Fab mutant (HC K129X, X = pAzF), which could serve as a nonrelevant antibody control for follow-up imaging experiments. Both Fab antibodies migrated as a single band on SDS/PAGE analysis, indicating a >95% purity and a molecular weight of ~45 kDa (Figure S2). Their identities were further confirmed by ESI-MS analysis (Figure S3).

Synthesis and Characterization of Site-Specific NOTA-Anti-PD-L1 Fab Conjugate.

Next, we conjugated the purified Fab mutants (αPD-L1 Fab and αHER2 Fab, HC K129X, X = pAzF) with linker compound **4** (Figure 1A). Each pAzF-containing Fab was reacted with a 10-fold excess of NOTA–BCN linker at 37 °C for 12 h to ensure the complete conjugation.

The Fab conjugates were purified following the reported procedures[36,57] and analyzed by SDS/PAGE (Figure S2) and ESI-MS (Figure S3), which demonstrated that the final conjugates were >95% pure, and had the desired molecular mass with a NOTA-to-antibody ratio of 1 (Figure S3). The binding affinity of αPD-L1 Fab fragments to PD-L1 was evaluated by ELISA (Figure 1B). The conjugate and the HC-K129 mutant both have a similar affinity (EC_{50}'s ~ 0.7 nM) to the wild type, suggesting that neither the site-directed mutation nor payload conjugation at the selected site compromises the antibody's binding.

In Vivo PET Imaging of PD-L1 Expression.

To utilize this class of site-specific Fab conjugates as imaging probes, we evaluated their in vivo PET imaging capability using nude mice that are immuno-deficient and can potentially carry various tumor types for future studies.[58–60] After radiolabeling with ^{64}Cu, 50–70 μCi of either ^{64}Cu-NOTA-αPD-L1 or ^{64}Cu-NOTA-αHER2 were intravenously administered to nude mice. PET scans were performed at 5, 15, and 45 min postinjection (pi). As demonstrated by Figure 3A, PET signal vs noise became stable at 45 min pi, with background signals almost cleared. Compared to the intact full-length antibody counterparts,[10,23] Fab fragment-based PET agents provided higher contrast imaging due to the low level of nonspecific accumulation and faster clearance mechanisms,[61] potentially ideal for imaging highly abundant surface markers. Fab conjugates were mostly cleared through the renal pathway and excreted via the urinary bladder, as evidenced by the extremely high kidney and bladder uptakes. Both images (Figure 3A) and region-of-interest (ROI) analysis (Figure 3B,C) revealed specific uptake of ^{64}Cu-NOTA-αPD-L1 in brown adipose tissue (BAT) and spleen. For BAT, the accumulation of ^{64}Cu-NOTA-αPD-L1 was the highest immediately after injection (6.2 ± 2.4% ID/g, $n = 3$) and remained high throughout the study (6.1 ± 2.1% ID/g at 45 min). The control ^{64}Cu-NOTA-αHER2, on the contrary, displayed minimal enrichment in BAT, from 1.7 ± 0.2% ID/g at 15 min to 1.6 ± 0.1% ID/g at 45 min ($n = 3$). For the spleen, there was a similar trend for ^{64}Cu-NOTA-αPD-L1 (11.8 ± 3.0% ID/g at 15 min to 12.0 ± 1.9% ID/g at 45 min, $n = 3$), whereas the uptake of the control ^{64}Cu-NOTA-αHER2 (2.5 ± 0.1% ID/g at 15 min to 2.1 ± 0.3% ID/g at 45 min, $n = 3$) remained low. These resulted in statistically significant differences ($p < 0.05$) in both BAT and spleen uptake for the two imaging tracers at the time point of 45 min pi (Figure 3B,C), whereas there was no notable difference in other analyzed organs.

To further confirm that the observed enrichment of ^{64}Cu-NOTA-αPD-L1 is antigen-specific, we performed blocking studies in nude mice by injecting wild type αPD-L1 Fab at a dose of ~200 μg/mouse prior to the administration of the corresponding NOTA conjugate. As shown in Figure 3B,C, the uptake of the NOTA conjugate was drastically decreased in both BAT (1.9 ± 0.3% ID/g at 15 min and 1.4 ± 0.3% ID/g at 45 min, $n = 3$) and spleen (3.8 ± 0.3% ID/g at 15 min and 1.7 ± 1.2% ID/g at 45 min, $n = 3$), similar to the levels of the control αHER2 conjugate. Taken together, this set of results indicates that the uptake of PET tracer in BAT and spleen of nude mice was PD-L1 specific. This finding suggests that the ^{64}Cu-NOTA-αPD-L1 probe is a reliable, nonmetabolic tracer for in vivo PD-L1 expression. PD-L1 checkpoint was initially regarded to be primarily expressed in the extralymphatic organs.[3,10] The existence of PD-L1 in the spleen is consistent with recent findings that PD-L1 is additionally expressed in secondary lymphatic organs.[10] The presence of PD-L1 in BAT

further confirms that adipose tissue is influenced by the arms of the immune system.[10,21,62] These organs' expression of PD-L1 may suggest their utilization of PD-1/PD-L1 interactions to locally suppress unwanted T-cell responses.[10]

Next, we set out to gauge the general applicability of our imaging probe in another mouse model, C57BL/6 mice, that are immunocompetent. Similarly, the BAT and spleen were found to have a much higher accumulation of ^{64}Cu-NOTA-αPD-L1 than that of the control ^{64}Cu-NOTA-αHER2 throughout the study (Figure S4). The uptake of ^{64}Cu-NOTA-αPD-L1 in the spleen was less significant (Figure S4A,C), presumably due to the more varied expression levels of PD-L1 in the spleens among individual C57BL/6 mice (Figure S4A,C).[10,63,64] This observation may accurately reflect the real situation, which in translation to the clinical situation may partially account for heterogeneous immunotherapeutic responses.

Ex Vivo Biodistribution Studies and Immunofluorescence Staining.

Following the last PET scan at 90 min pi, C57BL/6 mice were sacrificed, with major organs resected for ex vivo γ counting to corroborate the quantification of PET images (Figure S5). The kidneys from both groups had an extremely high accumulation of the tracers, at 157 ± 27% ID/g for ^{64}Cu-NOTA-αPD-L1 and 219 ± 28% ID/g for ^{64}Cu-NOTA-αHER2. Low but specific tracer uptake in the lung and intestines were also revealed, consistent with the reported PD-L1 expression in minor cell populations.[10] Notably, the biodistribution data corroborated the findings from in vivo PET ROI analysis. The BAT uptakes with the two imaging agents were significantly different from one another in this analysis as well (4.5 ± 1.5% ID/g for ^{64}Cu-NOTA-αPD-L1 and 0.9 ± 0.2% ID/g for ^{64}Cu-NOTA-αHER2, $p < 0.05$). The enrichment of ^{64}Cu-NOTA-αPD-L1 was still higher than the control in the spleen (9.4 ± 3.9 vs 2.3 ± 0.8% ID/g) but with large variations. Follow-up immunofluorescent staining of these organs further confirmed that both BAT and spleen are PD-L1 positive (Figure 4). These results are consistent with the recent literature reports,[9,10,21,24,26] which suggests the tissue-specific (BAT, spleen) uptake of antibodies against PD-L1 and indicates that our ^{64}Cu-NOTA-αPD-L1 probe is highly specific toward PD-L1.

CONCLUSIONS

We have developed and studied a ^{64}Cu-labeled, UAA-based, site-specific Fab conjugate as an imaging probe to measure PD-L1 expression levels in vivo with immuno-PET. This antibody conjugate was optimized at a fixed site and stoichiometry and bears an indistinguishable binding affinity from the unconjugated wild type toward the cognate antigen. When applied to noninvasive in vivo imaging, the probe can sensitively detect the expression levels of the targeted antigen, in different mouse models. The particular PD-L1 expression on nontumor organs, such as BAT, lung, and intestines, as revealed by this probe, may indicate that targeted T-cell responses in these organs are strongly suppressed by the PD-1/PD-L1 immune checkpoint.[10] Further, these findings may explain the frequent association of immune checkpoint blockade with immune-related adverse effects on these organs,[10] underlying the importance of image-guided prognosis and treatment monitoring in immunotherapy. These data generally support the hypothesis that imaging PD-L1 expression with UAA-based site-specific Fab conjugates may be feasible in future clinical settings.

Further evaluation of the conjugate in disease-related models (xenograft and syngeneic tumor models) will be required to determine its clinical potential. In addition, we are comparing the properties and activity of this conjugate with random conjugates and cysteine-based site-specific conjugates. Finally, this work suggests that the amber suppression-mediated genetic incorporation strategy has applicability as a route to a class of site-specific immuno-PET probes that can potentially guide immune checkpoint-targeted immunotherapy.

Supplementary Material

Refer to Web version on PubMed Central for supplementary material.

ACKNOWLEDGMENTS

This work was supported by grant #15-175-22 from the American Cancer Society, Temple University Startup Fund, and was also supported, in part, by the University of Wisconsin-Madison and the National Institutes of Health (P30CA014520, T32GM008505, T32CA009206). V.A.V. and S.Z. were supported by National Institutes of Health (NIH) grant 1R01GM123296.

REFERENCES

(1). Burugu S; Dancsok AR; Nielsen TO Emerging targets in cancer immunotherapy. Semin. Cancer Biol. 2018, 52, 39–52.

(2). Davies M; Duffield EA Safety of checkpoint inhibitors for cancer treatment: strategies for patient monitoring and management of immune-mediated adverse events. ImmunoTargets Ther. 2017, 6, 51–71. [PubMed: 28894725]

(3). Pardoll DM The blockade of immune checkpoints in cancer immunotherapy. Nat. Rev. Cancer 2012, 12, 252–264. [PubMed: 22437870]

(4). Aris M; Mordoh J; Barrio MM Immunomodulatory Monoclonal Antibodies in Combined Immunotherapy Trials for Cutaneous Melanoma. Front. Immunol. 2017, 8, No. 1024. [PubMed: 28970830]

(5). Voutsadakis IA Immune Blockade Inhibition in Breast Cancer. Anticancer Res. 2016, 36, 5607–5622. [PubMed: 27793883]

(6). Moslehi JJ; Salem JE; Sosman JA; Lebrun-Vignes B; Johnson DB Increased reporting of fatal immune checkpoint inhibitor-associated myocarditis. Lancet 2018, 391, 933.

(7). Johnson DB; Balko JM; Compton ML; Chalkias S; Gorham J; Xu Y; Hicks M; Puzanov I; Alexander MR; Bloomer TL; Becker JR; Slosky DA; Phillips EJ; Pilkinton MA; Craig-Owens L; Kola N; Plautz G; Reshef DS; Deutsch J5 ; Deering RP; Olenchock BA; Lichtman AH; Roden DM; Seidman CE; Koralnik IJ; Seidman JG; Hoffman RD; Taube JM; Diaz LA Jr.; Anders RA; Sosman JA; Moslehi JJ Fulminant Myocarditis with Combination Immune Checkpoint Blockade. N. Engl. J. Med. 2016, 375, 1749–1755. [PubMed: 27806233]

(8). Leem G; Song SY Immunotherapy in Pancreatic Cancer; the Road Less Traveled. Immunol. Disord. Immunother. 2016, 1, No. 1000106.

(9). Ingram JR; Dougan M; Rashidian M; Knoll M; Keliher EJ; Garrett S; Garforth S; Blomberg OS; Espinosa C; Bhan A; Almo SC; Weissleder R; Lodish H; Dougan SK; Ploegh HL PD-L1 is an activation-independent marker of brown adipocytes. Nat. Commun. 2017, 8, No. 647. [PubMed: 28935898]

(10). Hettich M; Braun F; Bartholoma MD; Schirmbeck R; Niedermann G High-Resolution PET Imaging with Therapeutic Antibody-based PD-1/PD-L1 Checkpoint Tracers. Theranostics 2016, 6, 1629–1640. [PubMed: 27446497]

(11). Natarajan A; Mayer AT; Xu L; Reeves RE; Gano J; Gambhir SS Novel Radiotracer for ImmunoPET Imaging of PD-1 Checkpoint Expression on Tumor Infiltrating Lymphocytes. Bioconjugate Chem. 2015, 26, 2062–2069.

(12). Rom-Jurek E-M; Kirchhammer N; Ugocsai P; Ortmann O; Wege AK; Brockhoff G Regulation of Programmed Death Ligand 1 (PD-L1) Expression in Breast Cancer Cell Lines In Vitro and in Immunodeficient and Humanized Tumor Mice. Int. J. Mol. Sci. 2018, 19, No. 563.

(13). Sabatier R; Finetti P; Mamessier E; Adelaide J; Chaffanet M; Ali HR; Viens P; Caldas C; Birnbaum D; Bertucci F Prognostic and predictive value of PDL1 expression in breast cancer. Oncotarget 2015, 6, 5449–5464. [PubMed: 25669979]

(14). Ehlerding EB; England CG; McNeel DG; Cai W Molecular Imaging of Immunotherapy Targets in Cancer. J. Nucl. Med. 2016, 57, 1487–1492. [PubMed: 27469363]

(15). Bauckneht M; Piva R; Sambuceti G; Grossi F; Morbelli S Evaluation of response to immune checkpoint inhibitors: Is there a role for positron emission tomography? World J. Radiol. 2017, 9, 2733.

(16). Widmann G; Nguyen VA; Plaickner J; Jaschke W Imaging Features of Toxicities by Immune Checkpoint Inhibitors in Cancer Therapy. Curr. Radiol. Rep. 2017, 5, 59.

(17). Huisman M; Menke C; Gootjes E; Vugts D; Greuter H; Boellaard R; Verheul H; Van Dongen G 89Zr labeled cetuximab imaging in colorectal cancer patients aimed at image-guided patient selection for anti-EGFR treatment. J. Nucl. Med. 2014, 55, 225.

(18). Menke-van der Houven van Oordt CW; Gootjes EC; Huisman MC; Vugts DJ; Roth C; Luik AM; Mulder, ER; Schuit RC; Boellaard R; Hoekstra OS; van Dongen GA; Verheul HM 89Zr-cetuximab PET imaging in patients with advanced colorectal cancer. Oncotarget 2015, 6, 30384–30393. [PubMed: 26309164]

(19). van Dijk LK; Boerman OC; Kaanders JH; Bussink J PET Imaging in Head and Neck Cancer Patients to Monitor Treatment Response: A Future Role for EGFR-Targeted Imaging. Clin. Cancer Res. 2015, 21, 3602–3609. [PubMed: 25931452]

(20). Chatterjee S; Lesniak WG; Nimmagadda S Noninvasive Imaging of Immune Checkpoint Ligand PD-L1 in Tumors and Metastases for Guiding Immunotherapy. Mol. Imaging 2017, 16, No. 1536012117718459. [PubMed: 28707500]

(21). Chatterjee S; Lesniak WG; Gabrielson M; Lisok A; Wharram B; Sysa-Shah P; Azad BB; Pomper MG; Nimmagadda S A humanized antibody for imaging immune checkpoint ligand PD-L1 expression in tumors. Oncotarget 2016, 7, 10215–10227. [PubMed: 26848870]

(22). England CG; Jiang D; Ehlerding EB; Rekoske BT; Ellison PA; Hernandez R; Barnhart TE; McNeel DG; Huang P; Cai W (89)Zr-labeled nivolumab for imaging of T-cell infiltration in a humanized murine model of lung cancer. Eur. J. Nucl. Med. Mol. Imaging 2018, 45, 110–120. [PubMed: 28821924]

(23). Heskamp S; Hobo W; Molkenboer-Kuenen JD; Olive D; Oyen WJ; Dolstra H; Boerman OC Noninvasive Imaging of Tumor PD-L1 Expression Using Radiolabeled Anti-PD-L1 Antibodies. Cancer Res. 2015, 75, 2928–2936. [PubMed: 25977331]

(24). Josefsson A; Nedrow JR; Park S; Banerjee SR; Rittenbach A; Jammes F; Tsui B; Sgouros G Imaging, Biodistribution, and Dosimetry of Radionuclide-Labeled PD-L1 Antibody in an Immunocompetent Mouse Model of Breast Cancer. Cancer Res. 2016, 76, 472–479. [PubMed: 26554829]

(25). Natarajan A; Mayer AT; Reeves RE; Nagamine CM; Gambhir SS Development of Novel ImmunoPET Tracers to Image Human PD-1 Checkpoint Expression on Tumor-Infiltrating Lymphocytes in a Humanized Mouse Model. Mol. Imaging Biol. 2017, 19, 903–914. [PubMed: 28247187]

(26). Truillet C; Oh HLJ; Yeo SP; Lee CY; Huynh LT; Wei J; Parker MFL; Blakely C; Sevillano N; Wang YH; Shen YS; Olivas V; Jami KM; Moroz A; Jego B; Jaumain E; Fong L; Craik CS; Chang AJ; Bivona TG; Wang CI; Evans MJ Imaging PD-L1 Expression with ImmunoPET. Bioconjugate Chem. 2018, 29, 96–103.

(27). Ilovich O; Natarajan A; Hori S; Sathirachinda A; Kimura R; Srinivasan A; Gebauer M; Kruip J; Focken I; Lange C; Carrez C; Sassoon I; Blanc V; Sarkar SK; Gambhir SS Development and Validation of an Immuno-PET Tracer as a Companion Diagnostic Agent for Antibody-Drug Conjugate Therapy to Target the CA6 Epitope. Radiology 2015, 276, 191–198. [PubMed: 25734548]

(28). Maute RL; Gordon SR; Mayer AT; McCracken MN; Natarajan A; Ring NG; Kimura R; Tsai JM; Manglik A; Kruse AC; Gambhir SS; Weissman IL; Ring AM Engineering high-affinity PD-1 variants for optimized immunotherapy and immuno-PET imaging. Proc. Natl. Acad. Sci. U.S.A 2015, 112, E6506–E6514. [PubMed: 26604307]

(29). Adumeau P; Sharma SK; Brent C; Zeglis BM Site-Specifically Labeled Immunoconjugates for Molecular Imaging–Part 2: Peptide Tags and Unnatural Amino Acids. Mol. Imaging Biol. 2016, 18, 153–165. [PubMed: 26754791]

(30). Adumeau P; Sharma SK; Brent C; Zeglis BM Site-Specifically Labeled Immunoconjugates for Molecular Imaging–Part 1: Cysteine Residues and Glycans. Mol. Imaging Biol. 2016, 18, 1–17.

(31). Frutos S; Hernandez JL; Otero A; Calvis C; Adan J; Mitjans F; Vila-Perello M Site-Specific Antibody Drug Conjugates Using Streamlined Expressed Protein Ligation. Bioconjugate Chem. 2018, 29, 3503–3508.

(32). Muir TW Semisynthesis of proteins by expressed protein ligation. Annu. Rev. Biochem. 2003, 72, 249–289. [PubMed: 12626339]

(33). Wang L; Xie J; Schultz PG Expanding the genetic code. Annu. Rev. Biophys. Biomol Struct. 2006, 35, 225–249. [PubMed: 16689635]

(34). Liu CC; Schultz PG Adding new chemistries to the genetic code. Annu. Rev. Biochem. 2010, 79, 413–444. [PubMed: 20307192]

(35). Cao Y; Axup JY; Ma JS; Wang RE; Choi S; Tardif V; Lim RK; Pugh HM; Lawson BR; Welzel G; Kazane SA; Sun Y; Tian F; Srinagesh S; Javahishvili T; Schultz PG; Kim CH Multiformat T-cell-engaging bispecific antibodies targeting human breast cancers. Angew. Chem. Int. Ed. 2015, 54, 7022–7027.

(36). Lyu Z; Kang L; Buuh ZY; Jiang D; McGuth JC; Du J; Wissler HL; Cai W; Wang RE A Switchable Site-Specific Antibody Conjugate. ACS Chem. Biol. 2018, 13, 958–964. [PubMed: 29461804]

(37). Jackson D; Atkinson J; Guevara CI; Zhang C; Kery V; Moon SJ; Virata C; Yang P; Lowe C; Pinkstaff J; Cho H; Knudsen N; Manibusan A; Tian F; Sun Y; Lu Y; Sellers A; Jia XC; Joseph I; Anand B; Morrison K; Pereira DS; Stover D In vitro and in vivo evaluation of cysteine and site specific conjugated herceptin antibody-drug conjugates. PLoS One 2014, 9, No. e83865. [PubMed: 24454709]

(38). Tian F; Lu Y; Manibusan A; Sellers A; Tran H; Sun Y; Phuong T; Barnett R; Hehli B; Song F; DeGuzman MJ; Ensari S; Pinkstaff JK; Sullivan LM; Biroc SL; Cho H; Schultz PG; DiJoseph J; Dougher M; Ma D; Dushin R; Leal M; Tchistiakova L; Feyfant E; Gerber HP; Sapra P A general approach to site- specific antibody drug conjugates. Proc. Natl. Acad. Sci. U.S.A 2014, 111, 1766–1771. [PubMed: 24443552]

(39). Wu Y; Zhu H; Zhang B; Liu F; Chen J; Wang Y; Wang Y ; Zhang Z; Wu L; Si L; Xu H; Yao T; Xiao S; Xia Q; Zhang L ; Yang Z; Zhou D Synthesis of Site-Specific Radiolabeled Antibodies for Radioimmunotherapy via Genetic Code Expansion. Bioconjugate Chem. 2016, 27, 2460–2468.

(40). Wu N; Kang CS; Sin I; Ren S; Liu D; Ruthengael VC; Lewis MR; Chong HS Promising bifunctional chelators for copper 64-PET imaging: practical (64)Cu radiolabeling and high in vitro and in vivo complex stability. J. Biol. Inorg. Chem. 2016, 21, 177–184. [PubMed: 26666778]

(41). Shokeen M; Anderson CJ Molecular imaging of cancer with copper-64 radiopharmaceuticals and positron emission tomography (PET). Acc. Chem. Res. 2009, 42, 832–841. [PubMed: 19530674]

(42). Nayak TK; Brechbiel MW Radioimmunoimaging with longer-lived positron-emitting radionuclides: potentials and challenges. Bioconjugate Chem 2009, 20, 825–841.

(43). Cutler CS; Hennkens HM; Sisay N; Huclier-Markai S; Jurisson SS Radiometals for combined imaging and therapy. Chem. Rev. 2013, 113, 858–883. [PubMed: 23198879]

(44). de Sá A; Bonnet CS; Geraldes CF; Toth E; Ferreira PM ; Andre JP Thermodynamic stability and relaxation studies of small, triaza-macrocyclic Mn(II) chelates. Dalton Trans. 2013, 42, 4522–4532. [PubMed: 23348796]

(45). Máté G; Simecek J; Pniok M; Kertesz I; Notni J; Wester HJ; Galuska L; Hermann P The influence of the combination of carboxylate and phosphinate pendant arms in 1,4,7-

triazacyclononane-based chelators on their 68Ga labelling properties. Molecules 2015, 20, 13112–13126. [PubMed: 26197305]

(46). Riss PJ; Kroll C; Nagel V; Rosch F NODAPA-OH and NODAPA-(NCS)n: synthesis, 68Ga-radiolabelling and in vitro characterisation of novel versatile bifunctional chelators for molecular imaging. Bioorg. Med. Chem. Lett. 2008, 18, 5364–5367. [PubMed: 18835159]

(47). Dommerholt J; van Rooijen O; Borrmann A; Guerra CF; Bickelhaupt FM; van Delft FL Highly accelerated inverse electron-demand cycloaddition of electron-deficient azides with aliphatic cyclooctynes. Nat. Commun. 2014, 5, No. 5378. [PubMed: 25382411]

(48). Stasiuk GJ; Tamang S; Imbert D; Poillot C; Giardiello M; Tisseyre C; Barbier EL; Fries PH; de Waard M; Reiss P; Mazzanti M Cell-permeable Ln(III) chelate-functionalized InP quantum dots as multimodal imaging agents. ACS Nano 2011, 5, 8193–8201. [PubMed: 21888430]

(49). Badescu G; Bryant P; Bird M; Henseleit K; Swierkosz J; Parekh V; Tommasi R; Pawlisz E; Jurlewicz K; Farys M; Camper N; Sheng X; Fisher M; Grygorash R; Kyle A; Abhilash A; Frigerio M; Edwards J; Godwin A Bridging disulfides for stable and defined antibody drug conjugates. Bioconjugate Chem. 2014, 25, 1124–1136.

(50). Qi J; Ye X; Ren G; Kan F; Zhang Y; Guo M; Zhang Z; Li D Pharmacological efficacy of anti-IL-1beta scFv, Fab and full- length antibodies in treatment of rheumatoid arthritis. Mol. Immunol. 2014, 57, 59–65. [PubMed: 24091292]

(51). Boyerinas B; Jochems C; Fantini M; Heery CR; Gulley JL; Tsang KY; Schlom J Antibody-Dependent Cellular Cytotoxicity Activity of a Novel Anti-PD-L1 Antibody Avelumab (MSB0010718C) on Human Tumor Cells. Cancer Immunol. Res. 2015, 3, 1148–1157. [PubMed: 26014098]

(52). Kim CH; Axup JY; Lawson BR; Yun H; Tardif V; Choi SH; Zhou Q; Dubrovska A; Biroc SL; Marsden R; Pinstaff J; Smider VV; Schultz PG Bispecific small molecule-antibody conjugate targeting prostate cancer. Proc. Natl. Acad. Sci. U.S.A 2013, 110, 17796–17801. [PubMed: 24127589]

(53). Axup JY; Bajjuri KM; Ritland M; Hutchins BM; Kim CH; Kazane SA; Halder R; Forsyth JS; Santidrian AF; Stafin K; Lu Y; Tran H; Seller AJ; Biroc SL; Szydlik A; Pinkstaff JK; Tian F; Sinha SC; Felding-Habermann B; Smider VV; Schultz PG Synthesis of site-specific antibody-drug conjugates using unnatural amino acids. Proc. Natl. Acad. Sci. U.S.A 2012, 109, 16101–16106. [PubMed: 22988081]

(54). Kern JC; Cancilla M; Dooney D; Kwasnjuk K; Zhang R; Beaumont M; Figueroa I; Hsieh S; Liang L; Tomazela D; Zhang J; Brandish PE; Palmieri A; Stivers P; Cheng M; Feng G; Geda P; Shah S; Beck A; Bresson D; Firdos J; Gately D; Knudsen N; Manibusan A; Schultz PG; Sun Y; Garbaccio RM Discovery of Pyrophosphate Diesters as Tunable, Soluble, and Bioorthogonal Linkers for Site-Specific Antibody-Drug Conjugates. J. Am. Chem. Soc. 2016, 138, 1430–1445. [PubMed: 26745435]

(55). Oller-Salvia B Genetic Encoding of a Non-Canonical Amino Acid for the Generation of Antibody-Drug Conjugates Through a Fast Bioorthogonal Reaction. J. Visualized Exp. 2018, No. 58066.

(56). Young DD; Young TS; Jahnz M; Ahmad I; Spraggon G; Schultz PG An evolved aminoacyl-tRNA synthetase with atypical polysubstrate specificity. Biochemistry 2011, 50, 1894–1900. [PubMed: 21280675]

(57). Wang RE; Liu T; Wang Y; Cao Y; Du J; Luo X; Deshmukh V; Kim CH; Lawson BR; Tremblay MS; Young TS; Kazane SA; Wang F; Schultz PG An immunosuppressive antibody-drug conjugate. J. Am. Chem. Soc. 2015, 137, 3229–3232. [PubMed: 25699419]

(58). Ehlerding EB; England CG; Jiang D; Graves SA; Kang L; Lacognata S; Barnhart TE; Cai W CD38 as a PET Imaging Target in Lung Cancer. Mol. Pharmaceutics 2017, 14, 2400–2406.

(59). Fliedner FP; Hansen AE; Jorgensen JT; Kjaer A The use of matrigel has no influence on tumor development or PET imaging in FaDu human head and neck cancer xenografts. BMC Med. Imaging 2016, 16, 5. [PubMed: 26762341]

(60). Luo H; England CG; Goel S; Graves SA; Ai F; Liu B; Theuer CP; Wong HC; Nickles RJ; Cai W ImmunoPET and Near-Infrared Fluorescence Imaging of Pancreatic Cancer with a Dual-Labeled Bispecific Antibody Fragment. Mol. Pharmaceutics 2017, 14, 1646–1655.

(61). Olafsen T; Wu AM Antibody vectors for imaging. Semin. Nucl Med. 2010, 40, 167–181. [PubMed: 20350626]

(62). DiSpirito JR; Mathis D Immunological contributions to adipose tissue homeostasis. Semin. Immunol. 2015, 27, 315–321. [PubMed: 26616665]

(63). Nedrow JR; Josefsson A; Park S; Ranka S; Roy S; Sgouros G Imaging of Programmed Cell Death Ligand 1: Impact of Protein Concentration on Distribution of Anti-PD-L1 SPECT Agents in an Immunocompetent Murine Model of Melanoma. J. Nucl. Med. 2017, 58, 1560–1566. [PubMed: 28522738]

(64). Tang H; Liang Y; Anders RA; Taube JM; Qiu X; Mulgaonkar A; Liu X; Harrington SM; Guo J; Xin Y; Xiong Y; Nham K; Silvers W; Hao G; Sun X; Chen M; Hannan R; Qiao J; Dong H; Peng H; Fu YX PD-L1 on host cells is essential for PD-L1 blockade-mediated tumor regression. J. Clin. Invest. 2018, 128, 580–588. [PubMed: 29337303]

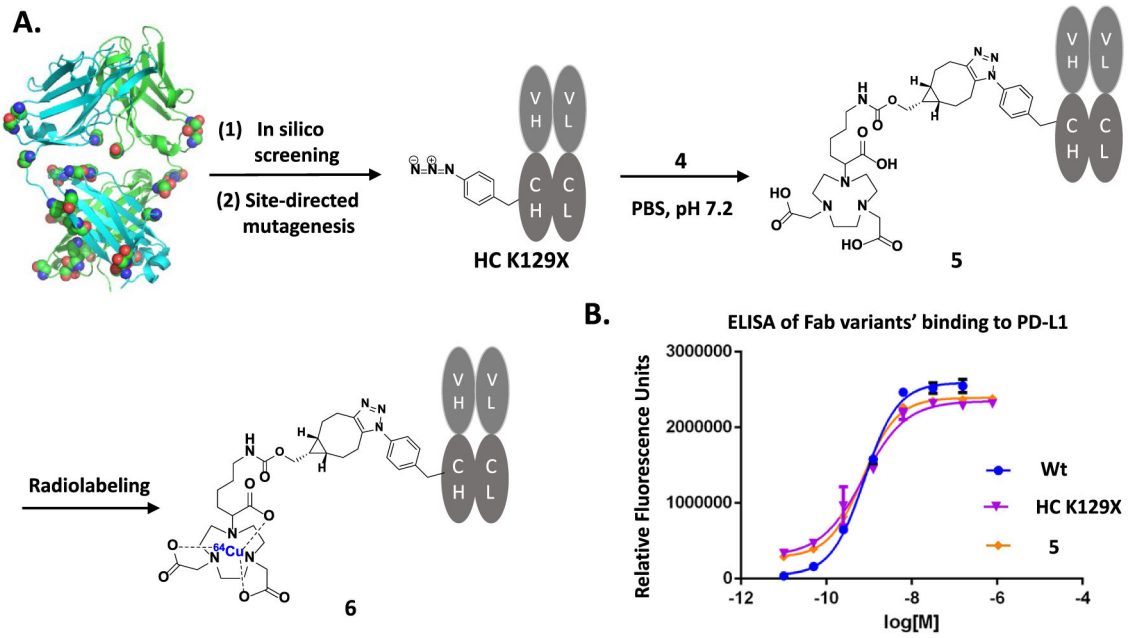

Figure 1.

Synthesis and characterization of the site-specific ^{64}Cu-NOTA-anti-PD-L1 Fab conjugate. (A) In silico screening with Rosetta has been performed with 23 solvent-exposed sites to determine the optimal mutation site, followed by site-directed mutagenesis to generate the anti-PD-L1 Fab (HC K129X, X = pAzF). Conjugation of this mutant with linker compound **4** will afford site-specific NOTA-anti-PD-L1 Fab conjugate **5** and its radiolabeled version, **6**. (B) Enzyme-linked immunosorbent assay (ELISA) analysis of the binding affinities of anti-PD-L1 Fab fragments. The EC_{50} was calculated to be 7.8×10^{-10} M for wild type, 7.3×10^{-10} M for the mutant (HC K129X, X = pAzF), and 7.2×10^{-10} M for conjugate **5**.

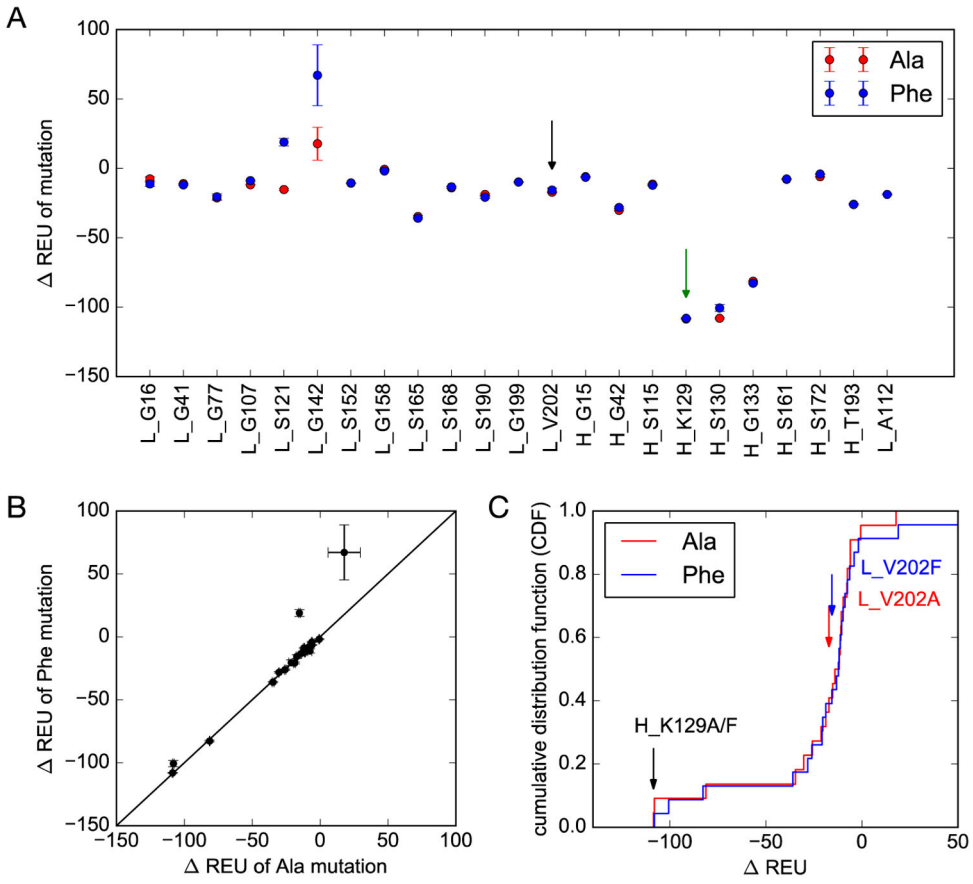

Figure 2.

In silico screening of mutation sites on αPD-L1 Fab. (A) Changes in stability ΔREU (Rosetta energy units) for single-residue mutations to alanine (red) and phenylalanine (blue). Error bars represent standard deviations in ΔREU across the 20 structures given by the RosettaBackrub algorithm. (B) Similar changes in stability were predicted for alanine and phenylalanine. (C) Cumulative histograms of the predicted score show that mutations at (heavy chain) H_K129 are predicted to be the most favorable of the 23 selected residues. Predictions for the chosen negative control (light chain) L_V202, in contrast, are not ranked as especially favorable.

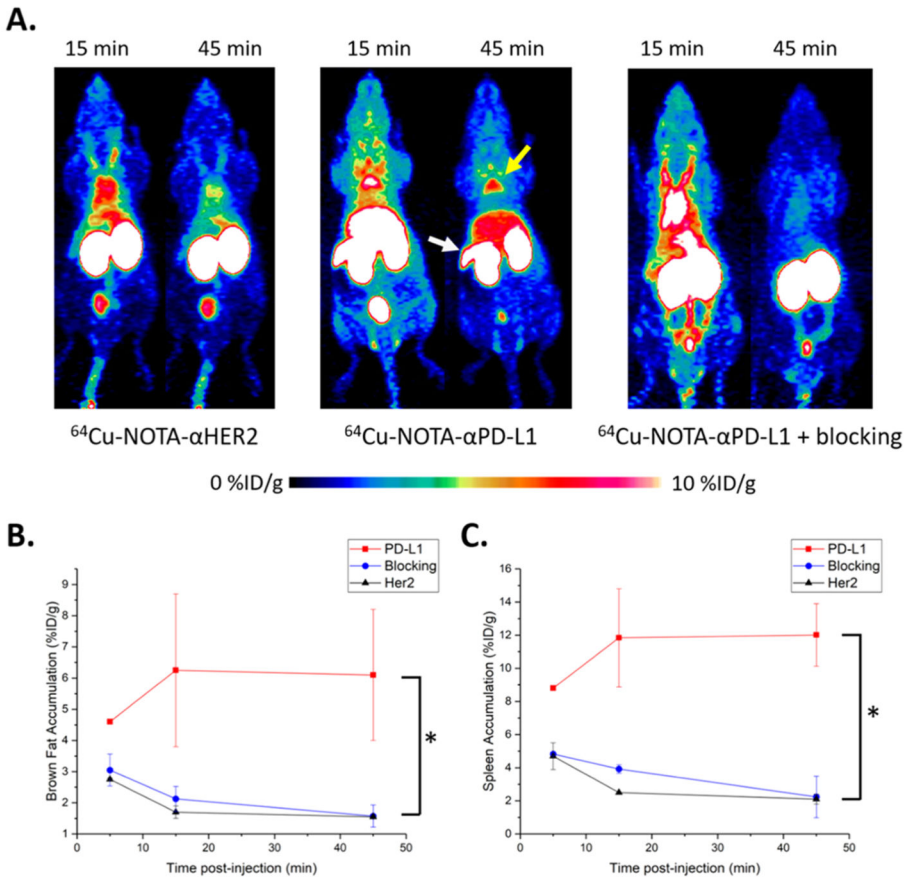

Figure 3.

In vivo PET imaging studies with ^{64}Cu-NOTA-αHER2 and ^{64}Cu-NOTA-αPD-L1 in nude mice. (A) PET scans at 15 and 45 min pi of ^{64}Cu-NOTA-αHER2 (left), ^{64}Cu-NOTA-αPD-L1 (middle), or ^{64}Cu-NOTA-αPD-L1 with preblocking by αPD-L1 w.t. (right); the yellow arrowhead indicates brown fat, whereas the white arrowhead points to the spleen. (B) Tracer uptake (% ID/g) for the three imaging groups in brown fat based on quantitative region-of-interest (ROI) analysis of the PET images. (C) Tracer uptake (% ID/g) in the spleen. "*" represents $p < 0.05$. $n = 3$.

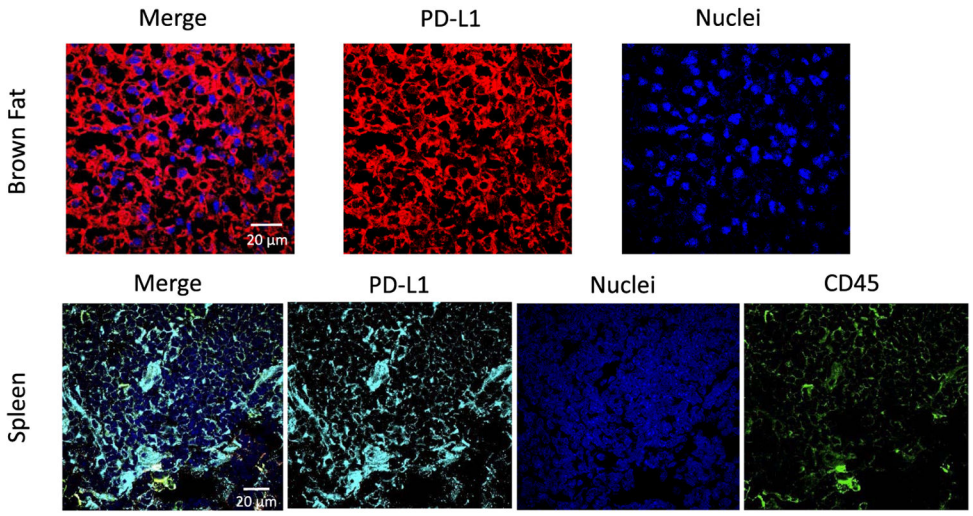

Figure 4.

Immunofluorescent staining of brown adipose tissue for PD-L1 expression (red) and spleen tissue for PD-L1 (cyan) and CD45 (green) expressions. Nuclei (blue) were stained as controls.

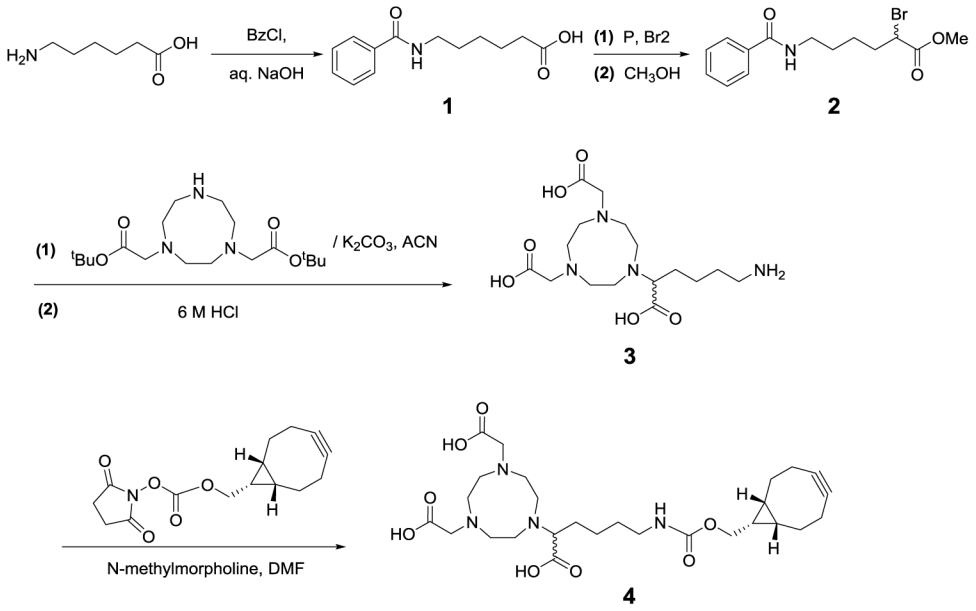

Scheme 1.

Synthetic Scheme of 1,4,7-Triazacyclononane-*N,N′,N″*-triacetic Acid (NOTA) Derivative with a (1*R*,8*S*,9*S*)-Bicyclo[6.1.0]non-4-yn-9-yl-methylcarbamate (BCN) Linker